

A discrete Boltzmann model with symmetric velocity discretization for compressible flow

Chuandong Lin(林传栋), Xiaopeng Sun(孙笑朋), Xianli Su(苏咸利), Huilin Lai(赖惠林), and Xiao Fang(方晓)
Citation: Chin. Phys. B, 2023, 32 (**11**): 110503. DOI: 10.1088/1674-1056/acea6b
Journal homepage: http://cpb.iphy.ac.cn; http://iopscience.iop.org/cpb

What follows is a list of articles you may be interested in

Performance optimization on finite-time quantum Carnot engines and refrigerators based on spin-1/2 systems driven by a squeezed reservoir

Haoguang Liu(刘浩广), Jizhou He(何济洲), and Jianhui Wang(王建辉)
Chin. Phys. B, 2023, 32 (**3**): 030503. DOI: 10.1088/1674-1056/aca207

Entanglement and thermalization in the extended Bose-Hubbard model after a quantum quench: A correlation analysis

Xiao-Qiang Su(苏晓强), Zong-Ju Xu(许宗菊), and You-Quan Zhao(赵有权)
Chin. Phys. B, 2023, 32 (**2**): 020506. DOI: 10.1088/1674-1056/ac76b1

Detection of multi-spin interaction of a quenched *XY* chain by the average work and the relative entropy

Xiu-Xing Zhang(张修兴), Fang-Jv Li(李芳菊), Kai Wang(王凯), Jing Xue(薛晶), Guang-Wen Huo(霍广文), Ai-Ping Fang(方爱平), and Hong-Rong Li(李宏荣)
Chin. Phys. B, 2021, 30 (**9**): 090504. DOI: 10.1088/1674-1056/abeef5

Nonequilibrium free energy and information flow of a double quantum-dot system with Coulomb coupling

Zhiyuan Lin(林智远), Tong Fu(付彤), Juying Xiao(肖菊英), Shanhe Su(苏山河), Jincan Chen(陈金灿), and Yanchao Zhang(张艳超)
Chin. Phys. B, 2021, 30 (**8**): 080501. DOI: 10.1088/1674-1056/abe119

A multiple-relaxation-time lattice Boltzmann method for high-speed compressible flows

Li Kai (李凯), Zhong Cheng-Wen (钟诚文)
Chin. Phys. B, 2015, 24 (**5**): 050501. DOI: 10.1088/1674-1056/24/5/050501

A discrete Boltzmann model with symmetric velocity discretization for compressible flow

Chuandong Lin(林传栋)[1,†], Xiaopeng Sun(孙笑朋)[1,‡], Xianli Su(苏咸利)[1,§], Huilin Lai(赖惠林)[2,¶], and Xiao Fang(方晓)[1,‖]

[1] *Sino-French Institute of Nuclear Engineering and Technology, Sun Yat-sen University, Zhuhai* 519082, *China*
[2] *School of Mathematics and Statistics, the Key Laboratory of Analytical Mathematics and Applications (Ministry of Education), Fujian Key Laboratory of Analytical Mathematics and Applications (FJKLAMA), and Center for Applied Mathematics of Fujian Province (FJNU), Fujian Normal University, Fuzhou* 350117, *China*

(Received 3 June 2023; revised manuscript received 12 July 2023; accepted manuscript online 26 July 2023)

A discrete Boltzmann model (DBM) with symmetric velocity discretization is constructed for compressible systems with an adjustable specific heat ratio in the external force field. The proposed two-dimensional (2D) nine-velocity scheme has better spatial symmetry and numerical accuracy than the discretized velocity model in literature [*Acta Aerodyn. Sin.* **40** 98108 (2022)] and owns higher computational efficiency than the one in literature [*Phys. Rev. E* **99** 012142 (2019)]. In addition, the matrix inversion method is adopted to calculate the discrete equilibrium distribution function and force term, both of which satisfy nine independent kinetic moment relations. Moreover, the DBM could be used to study a few thermodynamic nonequilibrium effects beyond the Euler equations that are recovered from the kinetic model in the hydrodynamic limit via the Chapman–Enskog expansion. Finally, the present method is verified through typical numerical simulations, including the free-falling process, Sod's shock tube, sound wave, compressible Rayleigh–Taylor instability, and translational motion of a 2D fluid system.

Keywords: discrete Boltzmann method, compressible flow, nonequilibrium effect, kinetic method

PACS: 05.70.Ln, 47.11.–j, 47.45.Ab, 51.10.+y **DOI:** 10.1088/1674-1056/acea6b

1. Introduction

Compressible flow with or without external force is of great importance in nature and a variety of engineering applications, such as high-speed aircraft, jet engines, rocket motors, entry into a planetary atmosphere, shock, and explosion.[1] Up to today, it remains a challenge to conduct in-depth research on compressible flow that often involves violent changes in physical fields, spatial and temporal multiscale behaviours, thermodynamic nonequilibrium (TNE) and hydrodynamic nonequilibrium (HNE) effects, among others. With the rapid development of computational fluid dynamics (CFD), numerical simulations have become a powerful tool for investigating fluid behaviours in either nearly incompressible or compressible complex systems, complementing the research conducted through pure experimentation and theory.[1] The fundamental basis of almost all CFD is the Navier–Stokes (NS) equations, which can be simplified by removing terms describing viscous actions to yield the Euler equations. Actually, both the NS and Euler models are based on the continuum assumption and primarily describe the HNE behaviours of the fluid system, but can not capture the essential accompanying TNE. As a transport equation describing the statistical behaviour of a thermodynamic system out of equilibrium, the Boltzmann equation can effectively incorporate both HNE and TNE information about the fluid systems.

At present, based on the Boltzmann equation, a series of simulation methods have been designed. One popular computational technique in association with the Boltzmann equation is the lattice Boltzmann method (LBM), which has been successfully developed for simulations of fluid phenomena.[2–14] The LBM research consists of two complementary branches. One aims to serve as a novel approach for numerically solving various partial differential equation(s). The other aims to act as an innovative method for constructing kinetic model to bridge the macro and micro descriptions. These two branches have distinct goals and consequently obey different rules.[15] For the first branch of LBM, a few examples are as follows. In 1998, Martys *et al*. derived a representation of the forcing term in the LBM based upon a Hermite expansion of the Boltzmann distribution function in velocity phase space.[2] In 2002, Guo *et al*. demonstrated that discrete lattice effects should be considered in the introduction of a force, and they designed a representation of the forcing term for the LBM, from which the NS equations could be obtained via the Chapman–Enskog

[†]Corresponding author. E-mail: linchd3@mail.sysu.edu.cn
[‡]Corresponding author. E-mail: sunxp6@mail2.sysu.edu.cn
[§]Corresponding author. E-mail: suxli@mail2.sysu.edu.cn
[¶]Corresponding author. E-mail: hllai@fjnu.edu.cn
[‖]Corresponding author. E-mail: fangx26@mail.sysu.edu.cn

© 2023 Chinese Physical Society and IOP Publishing Ltd

analysis.[3] In 2010, Mohamad and Kuzmin evaluated three different schemes for adding a force term to the LBM using the Bhatnager–Gross–Krook (BGK) method.[4] In 2018, Fei *et al*. used the central-moment-based collision operator and consistent forcing scheme for the three-dimensional LBM that significantly reduced computational costs.[9] It is worth noting that, as an optional numerical solver, the first branch of LBM aims to present a numerical solution of the traditional macroscopic governing equations of fluid mechanics, therefore its duty lies in being loyal to the original physical model.

As a variant version of the second branch of LBM, the discrete Boltzmann method (DBM) has emerged as a powerful tool for the research of compressible nonequilibrium phenomena during the last decade.[15–32] To be specific, the DBM possesses two remarkable merits. On the one hand, it can recover macroscopic fluid equations in the hydrodynamic limit and provide essential TNE information. On the other hand, the DBM is equivalent to a modified hydrodynamic model combined with a coarse-grained model that captures significant TNE behaviours when the physical system departs a bit far from equilibrium. In 2012, Xu *et al*. firstly pointed out that, under the condition that the based Boltzmann equation and the kinetic moments before discretization are consistent with those in nonequilibrium statistical physics, the non-conserved kinetic moments of the difference of distribution function f from its corresponding equilibrium $f^{\rm eq}$ can be used to measure the deviation of the system from its thermodynamic equilibrium and the resulting TNE effects.[16] This is the starting point of the current DBM.[15] In 2017, a two-component DBM was extended for compressible flows in the presence of a force field and utilized to study the effects of Reynolds numbers on the Rayleigh–Taylor (RT) instability.[21] In 2019, a multiple-relaxation-time DBM was developed for compressible thermal reactive flows, and an accurate matrix inversion method was adopted to calculate collision, reaction, and force terms.[24] In 2022, based on the ellipsoidal statistical BGK model, the DBM was developed for high-speed compressible flows, capturing various depths of TNE effects.[31] In the same year, a simplified DBM was presented, capable of recovering the reactive Euler equations in the continuum limit, and a 2D nine-velocity model was constructed, with the discrete velocities divided into three groups.[27] In brief, the current DBM stems from the second branch of LBM and focuses more on the TNE behaviors that the macro modeling generally ignore. It breaks through the continuity and near-equilibrium assumptions of traditional fluid modeling, discards the lattice gas image of standard LBM, and incorporates various methods based on phase space for checking, exhibiting, describing and analyzing the nonequilibrium state and resulting effects. More information extraction technologies and analysis methods for complex field are introduced over time.[15]

It should be pointed out that, after the physical model construction that is relatively fundamental, the next step involves the numerical design of a discrete scheme, which is another important issue directly related to the computational precision, robustness, and efficiency of simulations. For the kinetic model DBM, there are three aspects of discretization, i.e., the discretizing of time, space, and velocities. To solve the temporal and spatial derivatives in the discrete Boltzmann equation, researchers can adopt reasonable traditional or modified algorithms.[16] Furthermore, for the purpose of preliminary study on discrete velocities, in this paper, a 2D nine-velocity (D2V9) scheme is constructed for the DBM of compressible flow with external force. This discrete velocity scheme, named model (1, 4, 4), assumes a rest velocity, a group of velocities with the same magnitude $v_{\rm a}$ in four horizontal or vertical directions, and a group with size $v_{\rm b}$ in four diagonal directions. The proposed model exhibits greater spatial symmetry and numerical accuracy than the model (3, 3, 3) that includes three sets of discrete velocities with three directions in each group.[27] Besides, compared to the DBM using 2D sixteen-velocity (D2V16) composed of 4×4 discrete velocities and recovering the NS equations in the hydrodynamic limit,[24] the model with D2V9 offers higher computational efficiency but lower physical accuracy.

The rest of the paper is organized as follows. In Section 2, we introduce the DBM with the proposed discrete velocity model D2V9, utilize the matrix inversion method to calculate the equilibrium distribution function and force term, and show that the DBM could recover the Euler equations in the continuum limit and describe a few TNE effects beyond. In Section 3, the DBM is verified numerically through the benchmarks of the free-falling process, Sod's shock tube, sound wave, compressible RT instability, and translational motion of a 2D fluid system. Section 4 concludes the paper.

2. Discrete Boltzmann method

The BGK discrete Boltzmann equation takes the following form,

$$\frac{\partial f_i}{\partial t}+\boldsymbol{v}_i\cdot\nabla f_i=-\frac{1}{\tau}\left(f_i-f_i^{\rm eq}\right)+F_i, \tag{1}$$

where ∇ stands for the Hamilton operator, t the time, τ the relaxation time, f_i ($f_i^{\rm eq}$) the discrete (equilibrium) distribution function, F_i the force term, $i=1,2,\ldots,9$, the index of discrete Boltzmann velocity $\boldsymbol{v}_i$. Furthermore, from the discrete distribution function, the density ρ, hydrodynamic velocity $\boldsymbol{u}$, the energy E, and temperature T can be obtained by

$$\rho=\sum\nolimits_i f_i, \tag{2}$$

$$\rho\boldsymbol{u}=\sum\nolimits_i f_i\boldsymbol{v}_i, \tag{3}$$

$$E=\frac{1}{2}\rho u^2+\frac{1}{\gamma-1}\rho T=\frac{1}{2}\sum\nolimits_i f_i\left(v_i^2+\eta_i^2\right), \tag{4}$$

where $u=|\boldsymbol{u}|$ is the magnitude of the flow velocity, $v_i=|\boldsymbol{v}_i|$ denotes the magnitude of the discrete velocity, η_i accounts for the vibrational and/or rotational energies, and γ represents the specific heat ratio as follows:

$$\gamma=\frac{D+I+2}{D+I}, \tag{5}$$

in terms of the translational degrees of freedom D and extra degrees of freedom I. It is clear that this DBM can describe fluid systems with a flexible specific heat ratio as the parameter $D=2$ is fixed for a 2D system and I is tunable. It should be mentioned that the BGK-like models in various kinetic methods for nonequilibrium flow are not the original versions directly simplified from the Boltzmann equation, but are modified versions that have incorporated the mean-field theory description.[15]

Moreover, the matrix inversion method is adopted to calculate both discrete equilibrium distribution function and force term.[24] To be specific, the discrete equilibrium distribution function $f_i^{\rm eq}$ meets the following requirement:

$$\iint f^{\rm eq}\Psi \mathrm{d}\boldsymbol{v}\,\mathrm{d}\eta=\sum\nolimits_i f_i^{\rm eq}\Psi_i, \tag{6}$$

in terms of $\Psi=1,\ \boldsymbol{v},\ \left(\boldsymbol{v}\cdot\boldsymbol{v}+\eta^2\right),\ \boldsymbol{v}\boldsymbol{v},\ \left(\boldsymbol{v}\cdot\boldsymbol{v}+\eta^2\right)\boldsymbol{v}$, and corresponding elements $\Psi_i=1,\ \boldsymbol{v}_i,\ \left(\boldsymbol{v}_i\cdot\boldsymbol{v}_i+\eta_i^2\right),\ \boldsymbol{v}_i\boldsymbol{v}_i,\ \left(\boldsymbol{v}_i\cdot\boldsymbol{v}_i+\eta_i^2\right)\boldsymbol{v}_i$. Here the symbol $\boldsymbol{v}$ represents the molecular velocity, and η corresponds to its discrete counterpart η_i. In Eq. (6), the equilibrium distribution function $f^{\rm eq}$ can be expressed by[21]

$$f^{\rm eq}=\rho\left(\frac{1}{2\pi T}\right)^{D/2}\left(\frac{1}{2\pi IT}\right)^{1/2}\exp\left[-\frac{|\boldsymbol{v}-\boldsymbol{u}|^2}{2T}-\frac{\eta^2}{2IT}\right]. \tag{7}$$

Substituting Eq. (7) into Eq. (6) leads to the following five relations of kinetic moments:

$$\rho=\sum\nolimits_i f_i^{\rm eq}, \tag{8}$$

$$\rho u_\alpha=\sum\nolimits_i f_i^{\rm eq}v_{i\alpha}, \tag{9}$$

$$\rho\left[u^2+(D+I)T\right]=\sum\nolimits_i f_i^{\rm eq}\left(v_i^2+\eta_i^2\right), \tag{10}$$

$$\rho\left(\delta_{\alpha\beta}T+u_\alpha u_\beta\right)=\sum\nolimits_i f_i^{\rm eq}v_{i\alpha}v_{i\beta}, \tag{11}$$

$$\rho u_\alpha\left[(D+I+2)T+u^2\right]=\sum\nolimits_i f_i^{\rm eq}\left(v_i^2+\eta_i^2\right)v_{i\alpha}, \tag{12}$$

where u_α (u_β) is the component of flow velocity in the α (β) direction, and $v_{i\alpha}$ ($v_{i\beta}$) is the component of the discrete velocity in the α (β) direction. Equations (8)–(12) can be rewritten in the following form:

$$\hat{\boldsymbol{f}}^{\rm eq}=\boldsymbol{M}\ \boldsymbol{f}^{\rm eq}, \tag{13}$$

where $\boldsymbol{f}^{\rm eq}=\left(f_1^{\rm eq}\ f_2^{\rm eq}\ \cdots\ f_N^{\rm eq}\right)^{\rm T}$ is the column matrix of discrete equilibrium distribution functions, and $\hat{\boldsymbol{f}}^{\rm eq}=\left(\hat{f}_1^{\rm eq}\ \hat{f}_2^{\rm eq}\ \cdots\ \hat{f}_N^{\rm eq}\right)^{\rm T}$ denotes the column matrix of equilibrium kinetic moments $\hat{f}_1^{\rm eq}=\rho$, $\hat{f}_2^{\rm eq}=\rho u_x$, $\hat{f}_3^{\rm eq}=\rho u_y$, $\hat{f}_4^{\rm eq}=\rho\left[(D+I)T+u^2\right]$, $\hat{f}_5^{\rm eq}=\rho\left(T+u_x^2\right)$, $\hat{f}_6^{\rm eq}=\rho u_xu_y$, $\hat{f}_7^{\rm eq}=\rho\left(T+u_y^2\right)$, $\hat{f}_8^{\rm eq}=\rho u_x\left[(D+I+2)T+u^2\right]$, and $\hat{f}_9^{\rm eq}=\rho u_y\left[(D+I+2)T+u^2\right]$. Besides, the square matrix $\boldsymbol{M}$ is used to link the velocity space and moment space, with elements $M_{1i}=1$, $M_{2i}=v_{ix}$, $M_{3i}=v_{iy}$, $M_{4i}=v_i^2+\eta_i^2$, $M_{5i}=v_{ix}^2$, $M_{6i}=v_{ix}v_{iy}$, $M_{7i}=v_{iy}^2$, $M_{8i}=\left(v_i^2+\eta_i^2\right)v_{ix}$, and $M_{9i}=\left(v_i^2+\eta_i^2\right)v_{iy}$. If the matrix $\boldsymbol{M}$ is invertible, equation (13) can be written as

$$\boldsymbol{f}^{\rm eq}=\boldsymbol{M}^{-1}\ \hat{\boldsymbol{f}}^{\rm eq}, \tag{14}$$

where $\boldsymbol{M}^{-1}$ stands for the inverse matrix of $\boldsymbol{M}$.

In a similar way, the force term F_i satisfies the relationship as follows:

$$\iint F\Psi \mathrm{d}\boldsymbol{v}\,\mathrm{d}\eta=\sum\nolimits_i F_i\Psi_i, \tag{15}$$

where Ψ and Ψ_i are the same as those in Eq. (6), with

$$F=-\boldsymbol{a}\cdot\frac{\partial f}{\partial\boldsymbol{v}}\approx-\boldsymbol{a}\cdot\frac{\partial f^{\rm eq}}{\partial\boldsymbol{v}}=\frac{\boldsymbol{a}\cdot(\boldsymbol{v}-\boldsymbol{u})}{T}f^{\rm eq}, \tag{16}$$

which describes the variation rate of distribution function due to external force.[21,24] Physically, equation (16) is derived from the prerequisite that the equilibrium distribution function $f^{\rm eq}$ is the main portion of the distribution function f when the system is not too far from equilibrium. For a 2D coordinate system, equation (16) can be written as

$$F=\frac{f^{\rm eq}}{T}\left[a_x(v_x-u_x)+a_y(v_y-u_y)\right]. \tag{17}$$

Substituting Eq. (17) into Eq. (15) leads to

$$\hat{\boldsymbol{F}}=\boldsymbol{M}\ \boldsymbol{F}, \tag{18}$$

where $\boldsymbol{F}=\left(F_1\ F_2\ \cdots\ F_N\right)^{\rm T}$ stands for the column matrix of the force term in velocity space, and $\hat{\boldsymbol{F}}=\left(\hat{F}_1\ \hat{F}_2\ \cdots\ \hat{F}_N\right)^{\rm T}$ represents the column matrix of the force term in moment space, with elements $\hat{F}_1=0$, $\hat{F}_2=\rho a_x$, $\hat{F}_3=\rho a_y$, $\hat{F}_4=2\rho u_xa_x+2\rho u_ya_y$, $\hat{F}_5=2\rho u_xa_x$, $\hat{F}_6=\rho u_xa_y+\rho u_ya_x$, $\hat{F}_7=2\rho u_ya_y$, $\hat{F}_8=2\rho u_x(u_xa_x+u_ya_y)+\rho a_xu^2+\rho a_x(D+I+2)T$, and $\hat{F}_9=2\rho u_y(u_xa_x+u_ya_y)+\rho a_yu^2+\rho a_y(D+I+2)T$. Then, the mathematical expression of the force term is expressed by

$$\boldsymbol{F}=\boldsymbol{M}^{-1}\ \hat{\boldsymbol{F}}. \tag{19}$$

Through the Chapman–Enskog multiscale expansion, it can be demonstrated that, under the conditions of Eqs. (13) and (18), the DBM can recover the Euler equations

$$\frac{\partial\rho}{\partial t}+\frac{\partial}{\partial r_\alpha}(\rho u_\alpha)=0, \tag{20}$$

$$\frac{\partial}{\partial t}(\rho u_\alpha)+\frac{\partial p}{\partial r_\alpha}+\frac{\partial}{\partial r_\beta}\left(\rho u_\alpha u_\beta\right)=\rho a_\alpha, \tag{21}$$

$$\frac{\partial E}{\partial t}+\frac{\partial}{\partial r_\alpha}\left(Eu_\alpha+pu_\alpha\right)=\rho u_\alpha a_\alpha, \tag{22}$$

in the continuum limit. Here $p = \rho T$ is the pressure, r denotes the position, a represents the acceleration, the subscripts α and β stand for indices of coordinates, and Einstein summation notation is applied.

In addition, due to the conservation of mass, momentum and energy, equations (8)–(10) still hold if $f_i^{\rm eq}$ are replaced with f_i. On the contrary, equations (11) and (12) may not balance, with $f_i^{\rm eq}$ substituted by f_i. In fact, the kinetic moments of the difference between f_i and $f_i^{\rm eq}$ reflect the deviation of a physical system from its equilibrium state. In other words, it is convenient in the DBM to offer the following TNE manifestations:

$$\Delta_{2,\alpha\beta} = \sum\nolimits_i \left(f_i - f_i^{\rm eq}\right) v_{i\alpha} v_{i\beta}, \tag{23}$$

$$\Delta_{\alpha} = \sum\nolimits_i \left(f_i - f_i^{\rm eq}\right) \left(v_i^2 + \eta_i^2\right) v_{i\alpha}. \tag{24}$$

Mathematically, $\Delta_{2,\alpha\beta}$ is a second-order tensor with three independent variables $\Delta_{2,xx}$, $\Delta_{2,xy}$, and Δ_{2yy}. The symbol Δ_α denotes a vector with two components Δ_x and Δ_y. Physically, $\Delta_{2,\alpha\beta}$ is associated with the non-organized energy, and Δ_α is relevant to the non-organized energy flux in the α direction. In particular, the nonequilibrium quantity $\Delta_{2,xx}$ reflects the derivation of the translational energy in the x degree from equilibrium state, and $\Delta_{2,yy}$ reflects the departure of the translational energy in the y degree from equilibrium.

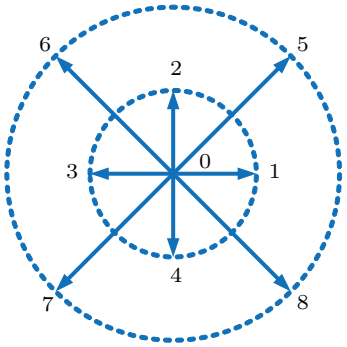


Fig. 1. Sketch of the discrete velocity model.

At this point, we have proposed a discrete Boltzmann model that can not only recover the Euler equations, but also capture some TNE effects. After the construction of the physical model, the next step is the numerical design of appropriate discretization schemes. In this work, the second-order Runge–Kutta scheme is chosen for the time derivative in Eq. (1), and the nonoscillatory nonfree dissipative scheme that is at the level of the second-order accuracy is adopted for the spatial derivative.[33] Furthermore, we construct a discrete velocity model, D2V9, in the following mathematical form:

$$\boldsymbol{v}_i = \begin{cases} (0,0), & i = 0, \\ v_{\rm a}\left[\cos\dfrac{(i-1)\pi}{2}, \sin\dfrac{(i-1)\pi}{2}\right], & 1 \le i \le 4, \\ v_{\rm b}\left[\cos\dfrac{(2i-1)\pi}{4}, \sin\dfrac{(2i-1)\pi}{4}\right], & 5 \le i \le 8, \end{cases} \tag{25}$$

where $(0,0)$ stands for the resting velocity, and the tunable parameters $v_{\rm a}$ and $v_{\rm b}$ are used to control the values of non-zero discrete velocities. Figure 1 depicts the sketch of the discrete velocities, which include a motionless velocity, four velocities with magnitude $v_{\rm a}$ in horizontal or vertical directions, and four velocities with size $v_{\rm b}$ in diagonal directions. Meanwhile, the variable η_i is introduced as follows:

$$\eta_i = \begin{cases} \eta_{\rm a}, & i = 0, \\ \eta_{\rm b}, & 1 \le i \le 4, \\ \eta_{\rm c}, & 5 \le i \le 8, \end{cases} \tag{26}$$

where $\eta_{\rm a}$, $\eta_{\rm b}$, and $\eta_{\rm c}$ are adjustable parameters.

It is noteworthy that the design of $\boldsymbol{v}_i$ and η_i has to ensure the invertibility of matrix $\boldsymbol{M}$ in order to apply the matrix inversion method. To achieve this, neither $v_{\rm a}$ or $v_{\rm b}$ can be zero (i.e., $v_{\rm a} \neq 0$ and $v_{\rm b} \neq 0$), and not all parameters of $\eta_{\rm a}$, $\eta_{\rm b}$, and $\eta_{\rm c}$ are zero (i.e., $|\eta_{\rm a}| + |\eta_{\rm b}| + |\eta_{\rm c}| > 0$). In addition, for the sake of better numerical robustness, the sizes of $\boldsymbol{v}_i$ and η_i can be adjusted to optimize the properties of the model.[26] On the one hand, the values of $v_{\rm a}$ and $v_{\rm b}$ can be set based on the values of the flow velocity, the sound speed $v_{\rm s} = \sqrt{\gamma T}$, as well as the shock speed, etc. On the other hand, the parameters $\eta_{\rm a}$, $\eta_{\rm b}$, and $\eta_{\rm c}$ could be around the result of $\sqrt{IT}$ according to the equipartition of energy.

3. Simulation and verification

In this section, let us carry out numerical simulations to test the DBM with the proposed discrete velocity scheme. To this end, we consider five typical benchmarks, i.e., the free-falling process, Sod's shock tube, sound wave, compressible RT instability, and translational motion of a 2D fluid system.

3.1. The free-falling process

First of all, the free-falling process of a physical system is adopted to verify the effectiveness of the force term. The system is homogeneous in a gravity field. Initially, the density is $\rho = 1.0$, the flow velocity $\boldsymbol{u} = 0$, and the temperature $T = 1.0$. Due to the external force, it falls with acceleration a_y in the y direction as time goes on. The specific heat ratio is $\gamma = 1.4$, the relaxation time $\tau = 4 \times 10^{-6}$, the temporal step $\Delta t = 10^{-6}$, the spatial step $\Delta x = \Delta y = 10^{-5}$, the mesh grid $N_x \times N_y = 1 \times 1$, and parameters $(v_{\rm a}, v_{\rm b}, \eta_{\rm a}, \eta_{\rm b}, \eta_{\rm c}) = (1.2, 2.0, 0.9, 3.0, 1.3)$. In addition, the periodic boundary condition is imposed on each boundary.

Figure 2 delineates the amplitude of vertical velocity u_y versus the value of acceleration a_y at a time instant $t = 0.01$ in the free-falling process. The squares represent the simulation results, and the solid line denotes the exact solution $u_y = a_y t$. Evidently, the DBM results are in excellent agreement with the exact solutions, hence it is confirmed that the matrix inversion method is accurate to calculate the external force on the right-hand of the discrete Boltzmann equation.

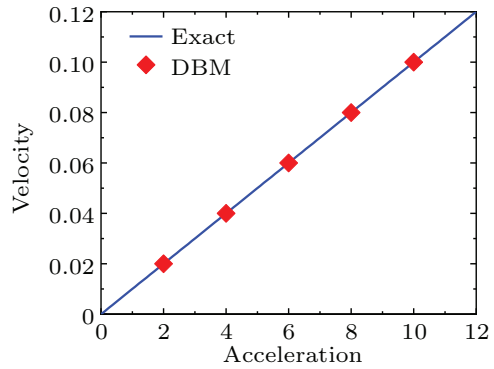


Fig. 2. Velocity versus acceleration in the free failing process.

3.2. Sod's shock tube

Next, the Sod's shock tube is simulated to verify that the DBM can be applied to compressible fluids. The initial configuration is

$$\begin{cases} (\rho, T, u_x, u_y)_{\mathrm{L}} = (0.15, 1.5, 0, 0), \\ (\rho, T, u_x, u_y)_{\mathrm{R}} = (0.125, 1.0, 0, 0), \end{cases} \tag{27}$$

where the subscript L denotes the left side $0 \le x < 0.075$ and R represents the right side $0.075 \le x \le 0.15$. In this simulation, the specific heat ratio is $\gamma = 2.0$, the relaxation time $\tau = 10^{-5}$, the temporal step $\Delta t = 2 \times 10^{-6}$, the spatial step $\Delta x = \Delta y = 5 \times 10^{-5}$, and the discrete parameters $v_{\mathrm{a}} = -3.5$, $v_{\mathrm{b}} = 1.2$, $\eta_{\mathrm{a}} = 4.0$, $\eta_{\mathrm{b}} = 0$, and $\eta_{\mathrm{c}} = 0$. In addition, the periodic boundary condition is employed for the top and bottom boundaries, and the inflow and outflow boundary conditions are selected in the left and right boundaries, respectively.

Figure 3 plots profiles of the density (a), pressure (b), temperature (c), and horizontal velocity (d) in the Sod's shock tube at the moment $t = 0.02$. Clearly, the leftmost is a rarefaction wave, the middle is a material interface, and the rightmost is a shock wave. The pressure and velocity keep constant while the density and temperature change across the material interface. All physical fields show remarkable gradients around the rarefaction or shock wave, and change sharply near the shock front. It can be found that the DBM results coincide with Riemann solutions on the whole. This indicates that the present DBM can be applied to compressible fluids.

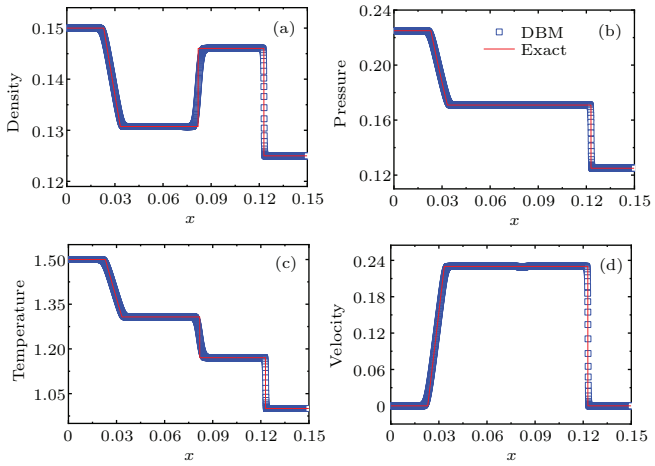


Fig. 3. Physical quantities in the Sod's shock tube: (a) density, (b) pressure, (c) temperature, and (d) horizontal velocity. The solid lines represent the Riemann solutions, and the squares stand for the DBM results.

Furthermore, let us test whether our DBM has the capability of describing TNE effects. Figure 4 depicts the nonequilibrium quantity $\Delta_{2,xx}$ in the Sod's shock tube at time $t = 0.03$. Subplot (a) illustrates the entire computational region, while subplots (b) and (c) show the areas around the rarefaction wave and shock wave, respectively. In each subplot, the results of D2V9, D2V16,[24] and theoretical solutions[26] are compared with each other. Firstly, it can be observed in Fig. 4(a) that the simulation results of both D2V9 and D2V16 agree with the analytical solutions on the whole. Secondly, the amplified domain in Fig. 4(b) shows that the D2V16 offers simulation results much closer to the theoretical solutions than D2V9. Thirdly, the amplified realm in Fig. 4(c) displays slight differences between all numerical and theoretical results.

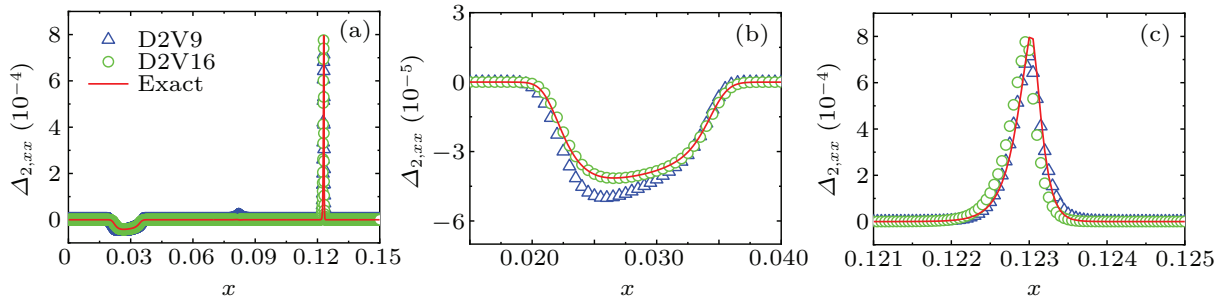


Fig. 4. The nonequilibrium quantity $\Delta_{2,xx}$ in the Sod's shock tube: (a) in the whole region, (b) across the rarefaction wave, and (c) around the shock wave. The triangles denote D2V9 results, the circles D2V16 results,[24] and the solid lines theoretical solutions.[26]

The physical reasons for the above phenomena are as follows. In the simplified DBM with D2V9, there are only 9 independent kinetic moment relations satisfied by the discrete equilibrium distribution function. On the contrary, for the DBM with D2V16, there are another 7 kinetic moment relations apart from those in the DBM with D2V9. That is to say, there are 16 independent moment relations satisfied by f_i^{eq} in the model of D2V16. The former DBM with D2V9 can recover the Euler equations in the continuum limit and capture a few TNE effects, while the latter model with D2V16 could

recover the NS equations in the hydrodynamic limit and offer more TNE information at a higher level of physical accuracy. Consequently, although both DBMs can provide quantities that are qualitatively correct, the model of D2V9 may involve larger errors than the one of D2V16. In fact, to achieve more accurate simulations in situations with various significant TNE effects, we can resort to a DBM where a larger number of moment relationships are required.[29,34]

3.3. Sound wave

In this part, the propagation of a sound wave is simulated in a physical system with the density $\rho_0 = 1.0$ and velocity $\boldsymbol{u}_0 = 0$. The relaxation time, temporal step, spatial step, and grid mesh are $\tau = \times 10^{-4}$, $\Delta t = 10^{-4}$, $\Delta x = \Delta y = 10^{-3}$, and $N_x \times N_y = 2000 \times 1$, respectively. Exerting a small perturbation at the initial position $x_0 = 0.2$ will result in the emergence of sound waves that propagate forwards and backwards, respectively. Additionally, the outflow boundary condition and periodic boundary condition are employed in the x and y directions, respectively.

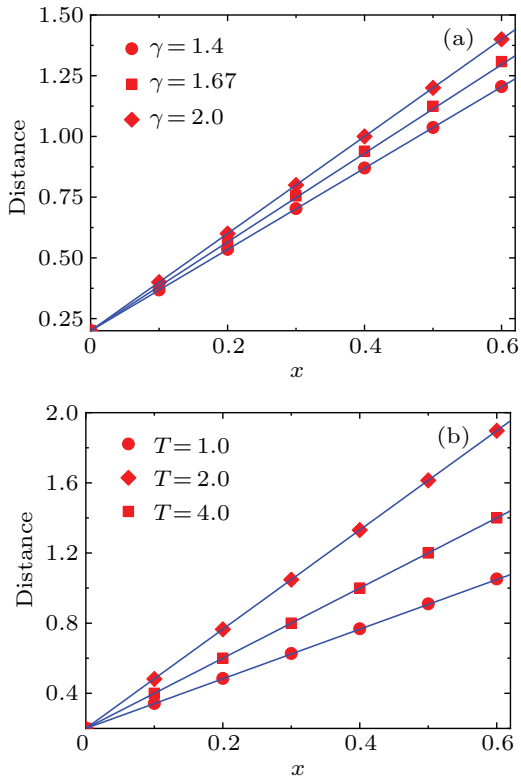


Fig. 5. Propagation of the sound wave with various specific heat ratios (a) and various temperatures (b).

Figure 5 displays the position of the sound wave travelling forwards in the evolution. The squares stand for simulation results of our DBM, and the solid lines indicate the theoretical solutions of $x = x_0 + v_s t$. Figure 5(a) shows results in three cases with different specific heat ratios γ and a constant temperature $T = 2.0$. Figure 5(b) gives cases of various temperatures and a fixed specific heat ratio $\gamma = 2.0$. Obviously, the numerical results agree well with the exact solutions. Therefore, the model is suitable for fluid systems with various temperatures and specific heat ratios.

3.4. The compressible RT instability

To further verify whether the DBM can effectively simulate complex fluids subjected to external force, we consider the compressible RT instability in a gravitational field. The computational domain, $[0,\ d] \times [-4d,\ 4d]$, is filled with two layers of fluids with different densities. Between the two media lies the material interface initially located at $y_c(x) = y_0 \cos(kx)$, where $k = 2\pi/\lambda$, $y_0 = 0.2d$, and $\lambda = 2d$ represent the wave number, the amplitude, and the wavelength, respectively. Initially, the whole system is in hydrostatic equilibrium,

$$\partial_y p(y) = -g\rho(y), \tag{28}$$

with g the magnitude of gravity acceleration. The initial pressure, which depends upon y, is given as follows:

$$\begin{cases} p(y) = p_0 \exp \dfrac{g(4d-y)}{T_u}, & y > 0, \\ p(y) = p_0 \exp\left(\dfrac{4gd}{T_u} - \dfrac{gy}{T_b}\right), & y < 0, \end{cases} \tag{29}$$

where p_0 is the initial pressure at the top of the fluid system, and T_u (T_b) denotes the initial temperature at the top (bottom). To smooth the transition between the interfaces, a layer is arranged between the two fluids with thickness $W = 0.03d$, and the initial temperature field is set as

$$T(x,y) = \frac{T_u + T_d}{2} + \frac{T_u - T_d}{2} \tanh \frac{y - y_c(x)}{W}, \tag{30}$$

where tanh denotes a hyperbolic tangent function. Then, the density field is obtained from the relation $\rho = p/T$. For the simulation, parameters are $p_0 = 3.53$, $\tau = 1 \times 10^{-5}$, $a_x = 0$, $a_y = -g = -1.0$, $T_u = 1.0$, and $T_b = 2.0$, $\Delta t = 5 \times 10^{-6}$, $\Delta x = \Delta y = 1.25 \times 10^{-4}$, and $N_x \times N_y = 250 \times 2000$. Moreover, the symmetric boundary condition is applied in the x and y directions.

Figure 6 exhibits the density contours in the evolution of RT instability at time instants $t = 0$, 0.5, 1.0, and 1.5, respectively. The left four snapshots are simulation results of the DBM with D2V9, while the right four snapshots are obtained using the model of D2V16. As shown in Fig. 6, the heavy (light) medium continuously sinks (rises) due to the gravity. With the passage of time, the vortex emerges and continues to develop in the later stage. The material interface becomes smooth and some fine fluid structures disappear as the two media penetrate into each other. It is confirmed that both models are capable of simulating the compressible RT instability and offer similar results with subtle differences. The simulation difference arises from the fact that, in the hydrodynamic limit, the former recovers the Euler equations, while the latter recovers the NS equations that contain dissipative effects of viscosity and heat conduction.

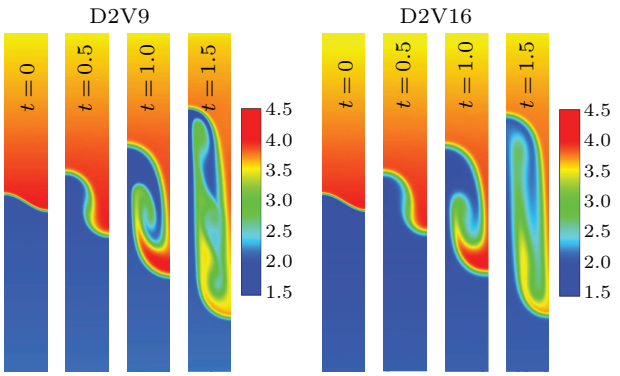


Fig. 6. Density contours in the evolution of RT instability simulated by the DBM with D2V9 (in the left four snapshots) and the model of D2V16 (in the right four snapshots).[24]

3.5. Translational motion

In this subsection, the movement of 2D fluid without considering external force is simulated to prove that the current model D2V9 (1, 4, 4) has better spatial symmetry and numerical robustness than the previous model D2V9 (3, 3, 3)[27] and possesses higher computational efficiency than D2V16.[24] Here the model (3, 3, 3) includes three sets of discrete velocities with three directions in each set,[27] and D2V16 contains fours groups of discrete velocities with four directions in each group.[24]

The computation area is a square in size $[0,d]\times[0,d]$, where a portion of fluid is placed around the center $(d/2,d/2)$ with a radius $R=d/4$. The inner and outer densities are $\rho_{\rm i}=1.1$ and $\rho_{\rm o}=1.0$, respectively, and there is a transition layer between the two parts. Mathematically, the density is set as follows:

$$\rho = \frac{\rho_{\rm i}+\rho_{\rm o}}{2}+\frac{\rho_{\rm i}-\rho_{\rm o}}{2} \times \tanh\frac{\sqrt{(x-d/2)^2+(y-d/2)^2}-R}{W}, \tag{31}$$

where $W=d/50$ is the thickness of the transition layer. The pressure is homogeneous in the system with $p=1.0$. Meanwhile, two types of flow are under consideration. One is moving rightwards, and the other is flowing in the diagonal direction. The initial configurations of the two cases are plotted in Figs. 7(a) and 7(b), respectively. Moreover, the periodic boundary condition is adopted, and simulation parameters are $d=0.02$, $\tau=4.0\times10^{-6}$, $\Delta t=2.0\times10^{-6}$, $\Delta x=\Delta y=1.0\times10^{-4}$, and $N_x\times N_y=200\times200$.

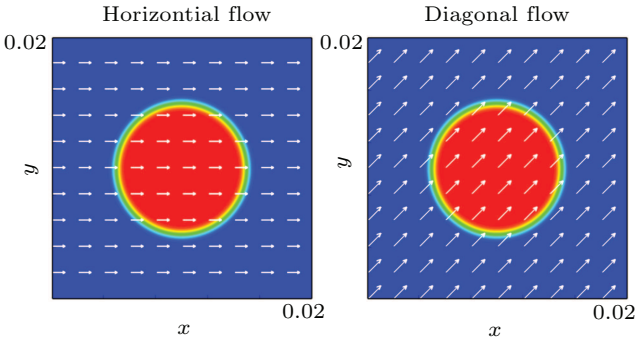


Fig. 7. The initial configurations of translational motion: horizontal flow (left) and diagonal flow (light).

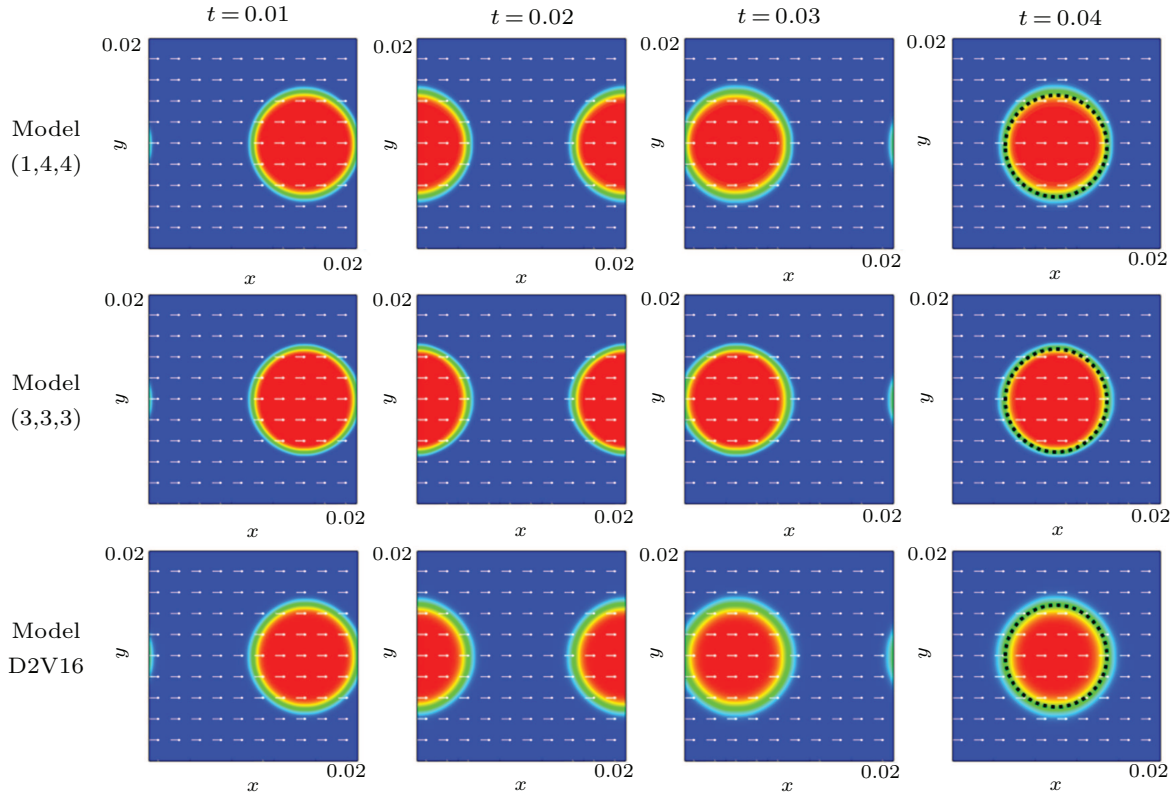


Fig. 8. The horizontal motion of fluid simulated by the models of D2V9 (1, 4, 4), D2V9 (3, 3, 3),[27] and D2V16,[24] in the three rows from top to bottom. The time instants are $t=0.01$, 0.02, 0.03, and 0.04 in the four columns from left to right.

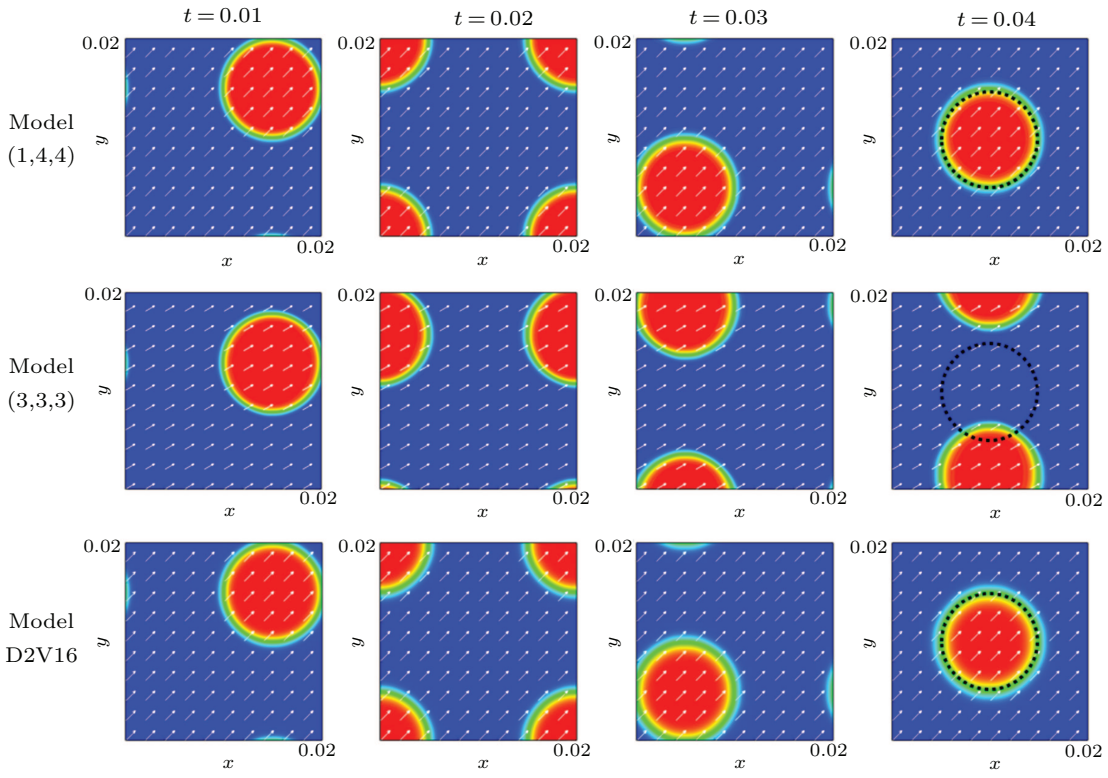


Fig. 9. The diagonal motion of fluid simulated by the models of D2V9 (1, 4, 4), D2V9 (3, 3, 3),[27] and D2V16,[24] in the three rows from top to bottom. The time instants are $t = 0.01$, 0.02, 0.03, and 0.04 in the four columns from left to right.

Figure 8 displays the snapshots of a horizontal flow system at four time instants $t = 0.01$, 0.02, 0.03, and 0.04 from left to right. The three rows of simulation results are given by using the models of D2V9 (1, 4, 4), D2V9 (3, 3, 3),[27] and D2V16,[24] respectively. In each subplot, the density reduces from red to blue, and the flow direction is marked with arrows. The dashed black circle in the last column is located at the initial position of the interface between the two media. Given an initial horizontal velocity $u_x = 0.5$ for the fluids, then it can be predicted that the system moves a distance $d = 0.02$ after a period of time $t = 0.04$, according to the relationship $u_x = d/t$ in theory.

It can be seen in Fig. 8 that the trajectories of the center of the fluid system provided by the three models are identical. The simulated material interface is symmetric about the centerline in the x direction and is close to the theoretical position on the dashed black curve. However, upon closer observation of subgraphs in the last column, slight differences can be found among the three simulation results at time $t = 0.04$. (i) In the first row, the dividing interface has little change in thickness, and its shape keeps quite close to a circle. (ii) In the second row, the contact area is wider in the x direction than in the y direction, and the shape seems an ellipse. (iii) In the last row, the material interface becomes wide gradually due to diffusion and its shape shows perfect symmetry.

In addition, we simulate the motion of a fluid system along the diagonal direction in Fig. 9. The components of flow velocity are $u_x = u_y = 0.5$, and the other conditions are the same as those in Fig. 8. It can be observed in Fig. 9 that the trajectory of the center follows the diagonal direction in both the first and last rows, while the center point departs farther and farther from the diagonal line over time. At the time instant $t = 0.04$, we can observe remarkable differences in the calculated results of the three models: (i) In the first row, the fluid moves in the diagonal direction, the material interface has little change in width, and its shape keeps close to a circle at the predetermined place. (ii) In the second row, the direction of flow velocity completely deviates from the predetermined direction, the contact area becomes wider in the horizontal direction than in the vertical direction, its location deviates far from the exact place, and its shape seems elliptical. (iii) In the last row, the fluid moves along a predetermined trajectory, the dividing boundary becomes thick, both the location and shape are correct.

From Figs. 8 and 9, it can be concluded that the models D2V9 (1, 4, 4) and D2V16 have higher physical accuracy and spatial symmetry than D2V9 (3, 3, 3). Moreover, it is worth noting that D2V9 of either (1, 4, 4) or (3, 3, 3) has a higher computational efficiency than D2V16. Table 1 shows the spatial symmetry and computational time of various discrete velocity models in simulations of the diagonal motion. The computation runs on a personal computer with the Intel(R) Core(TM) i7-8550U CPU @1.80 GHz. The computing time required by D2V9 (1, 4, 4) is close to that of the model (3, 3, 3), and is shorter than the one of D2V16. The computation time of D2V16 is about twice as much as that of

D2V9. Therefore, the current model D2V9 has a higher computational efficiency.

Table 1. Spatial symmetry and computational efficiency of various discrete velocity models.

Models	Spatial symmetry	Computing time (s)
D2V9 (1, 4, 4)	symmetry	539
D2V9 (3, 3, 3)	asymmetry	540
D2V16	symmetry	1171

4. Conclusion

In this work, a DBM with symmetric velocity discretization is presented for compressible flow system that is subjected to external force and possesses an adjustable specific heat ratio. We constructed a discrete velocity scheme, D2V9 (1, 4, 4), which assumes a resting velocity, a group of velocities with the same magnitude v_a in four horizontal or vertical directions, and a group with size v_b in four diagonal directions. This discretized velocity model has better spatial symmetry and numerical accuracy than the model in Ref. [27] and owns higher computational efficiency than the one in Ref. [24]. In addition, the matrix inversion method is adopted to calculate the discrete equilibrium distribution function and force term, both of which satisfy nine independent kinetic moment relations. Moreover, the DBM could be used to study a few thermodynamic nonequilibrium effects beyond the Euler equations that can be recovered from the kinetic model in the hydrodynamic limit via the Chapman–Enskog expansion. Finally, the method is verified through typical numerical simulations, including the free-falling process, Sod's shock tube, sound wave, compressible RT instability, and translational motion of a 2D fluid system. These simulations show that the current DBM can effectively investigate compressible flows with or without external force and could provide some nonequilibrium information.

Acknowledgements

Project supported by the National Natural Science Foundation of China (Grant Nos. 51806116, U2242214, and 11875329), Guangdong Basic and Applied Basic Research Foundation (Grant No. 2022A1515012116), and the Natural Science Foundation of Fujian Province, China (Grant Nos. 2021J01652 and 2021J01655).

References

[1] Anderson J D 2021 *Modern compressible flow: With historical perspective*, 4th edn. (Boston: McGraw-Hill) pp. 36–37
[2] Martys N S, Shan X W and Chen H D 1998 *Phys. Rev. E* **58** 6855
[3] Guo Z L, Zheng C G and Shi B C 2002 *Phys. Rev. E* **65** 046308
[4] Mohamad A and Kuzmin A 2010 *Int. J. Heat Mass Transfer* **53** 990996
[5] Zhang J F 2011 *Microfluid. Nanofluid.* **10** 128
[6] Li Q, Luo K H, Kang Q J, He Y L, Chen Q and Liu Q 2016 *Prog. Energy Combust. Sci.* **52** 62105
[7] Shan M L, Zhu C P, Yao C, Yin C and Jiang X Y 2016 *Chin. Phys. B* **25** 104701
[8] Sun D K, Chai Z H, Li Q and Lin G 2018 *Chin. Phys. B* **27** 088105
[9] Fei L L, Luo K H and Li Q 2018 *Phys. Rev. E* **97** 053309
[10] Zuo H, Deng S C and Li H B 2019 *Chin. Phys. B* **28** 030202
[11] Wang H, Tian F B and Liu X D 2022 *Chin. Phys. B* **31** 024701
[12] Bai L, Shan M L, Yang Y, Su N N, Qian J W and Han Q B 2022 *Chin. Phys. B* **31** 034701
[13] Zhong X G, Liu Y S, Yao Y C, He B and Wen B H 2023 *Chin. Phys. B* **32** 054701
[14] Qin F F, Fei L L, Zhao J L, Kang Q J, Derome D and Carmeliet J 2023 *J. Fluid Mech.* **963** A26
[15] Xu A G and Zhang Y D 2022 *Complex media kinetics* (Beijing: Science Press) pp. 67–229 (in Chinese)
[16] Xu A G, Zhang G C, Gan Y B, Chen F and Yu X J 2012 *Front. Phys.* **7** 582600
[17] Lin C D, Xu A G, Zhang G C, Li Y J and Succi S 2014 *Phys. Rev. E* **89** 013307
[18] Xu A G, Lin C D, Zhang G C and Li Y J 2015 *Phys. Rev. E* **91** 043306
[19] Lai H L, Xu A G, Zhang G C, Gan Y B, Ying Y J and Succi S 2016 *Phys. Rev. E* **94** 023106
[20] Lin C D, Xu A G, Zhang G C and Li Y J 2016 *Combust. Flame* **164** 137151
[21] Lin C D, Xu A G, Zhang G C, Luo K H and Li Y J 2017 *Phys. Rev. E* **96** 053305
[22] Lin C D and Luo K H 2018 *Combust. Flame* **198** 356362
[23] Lin C D and Luo K H 2018 *Comput. Fluids* **166** 176183
[24] Lin C D and Luo K H 2019 *Phys. Rev. E* **99** 012142
[25] Zhang Y D, Xu A G, Zhang G C, Gan Y B, Chen Z H and Succi S 2019 *Soft matter* **15** 22452259
[26] Lin C D, Luo K H, Xu A G, Gan Y B and Lai H L 2021 *Phys. Rev. E* **103** 013305
[27] Lin C D 2022 *Acta Aerodyn. Sin.* **40** 98108
[28] Gan Y B, Xu A G, Zhang G C and Succi S 2015 *Soft Matter* **11** 53365345
[29] Gan Y B, Xu A G, Zhang G C, Zhang Y D and Succi S 2018 *Phys. Rev. E* **97** 053312
[30] Ji Y, Lin C D and Luo K H 2022 *J. Comput. Phys.* **455** 111002
[31] Zhang D J, Xu A G, Zhang Y D, Gan Y B and Li Y J 2022 *Phys. Fluids* **34** 086104
[32] Zhang Y D, Xu A G, Zhang G C, Chen Z H and Wang P 2019 *Comput. Phys. Commun.* **238** 5065
[33] Zhang H X and Zhuang F G 1991 *Adv. Appl. Mech.* **29** 193256
[34] Gan Y B, Xu A G, Lai H L, Li W, Sun G L and Succi S 2022 *J. Fluid Mech.* **951** A8